Barnola, A.-S. and White, R.E. (2005).Coherence methods in mapping AVO anomalies and predicting P-wave and S-wave impedances. *Geophysical Prospecting* **53** (3), 423-433.

COHERENCE METHODS IN MAPPING AVO ANOMALIES AND PREDICTING P-WAVE AND S-WAVE IMPEDANCES

A-S. Barnola[1,2] and R.E.White[1]

[1]*Research School of Geological & Geophysical Sciences, Birkbeck College & University College London, South Wing UCL, Malet Place, London WC1E 6BT,UK.*
[2]*now at Beicip-Franlab, 232 avenue Napoléon-Bonaparte, 92500 Rueil-Malmaison, France.*

Email: A-Sophie.Barnola@ifp.fr

KEYWORDS

- Spectral coherence techniques;
- Quality control of AVO analysis/inversion;
- AVO anomaly mapping;
- AVO quantitative inversion.

ABSTRACT

Filters for migrated offset sub-stacks are designed by partial coherence analysis to predict "normal" AVO in an anomaly-free area. The same prediction filters generate localized prediction errors when applied in an AVO-anomalous interval. These prediction errors are quantitatively related to the AVO gradient anomalies in a background that is related to the minimum AVO anomaly detectable from the data. The prediction error section is thus used to define a reliability threshold for the identification of AVO anomalies. Coherence analysis also enables quality control of AVO analysis and inversion. For example, prediction that are non-localized and/or not showing structural conformity may indicate spatial variations in amplitude-offset scaling, seismic wavelet or signal-to-noise (S/N) ratio content. Scaling and waveform variations can be identified from inspection of the prediction filters and their frequency responses. S/N ratios can be estimated via multiple coherence analysis.

AVO inversion of seismic data is unstable if not constrained. However the use of a constraint on the estimated parameters has the undesirable effect of introducing biases into the inverted results: an additional bias correction step is then needed to retrieve unbiased results. An alternative form of AVO inversion that avoids additional corrections is proposed. This inversion is also fast as it only inverts AVO anomalies. A spectral coherence matching technique is employed to transform a zero-offset extrapolation or near-offset sub-stack into P-wave impedance. The same technique is applied to the prediction error section obtained by means of partial coherence, in order to estimate S-wave over P-wave velocity (V_S/V_P) ratios. Both techniques assume that one has accurate well ties and reliable density, P-wave and S-wave velocity logs and that impedance contrasts are not too strong. A full Zoeppritz inversion is required when too high impedance contrasts are encountered. An added assumption is made for the inversion to V_S/V_P ratio: the Gassmann fluid substitution theory is valid within the reservoir area. One synthetic example and one real North Sea inline illustrate the application of the two coherence methods.

INTRODUCTION

AVO analysis and inversion presents pitfalls when aimed at quantitatively characterizing the elastic properties of a reservoir. For instance a too poor S/N ratio could obscure any preliminary interpretation required for mapping. Moreover perfect absolute consistency in amplitude, timing and phase between migrated offset sub-stacks is unlikely ever to be realized. AVO analysis or inversion is likely to be biased by this lack of consistency. Then, although AVO inversion can be theoretically quantitative (Barnola and White 2001), in practice it remains very sensitive to noise. To overcome these pitfalls, we developed spectral matching techniques based on ordinary and partial coherence analyses. The advantage of these techniques is that only AVO anomalies are inverted. First normal, i.e. non-anomalous, AVO is predicted by partial coherence from migrated offset sub-stacks. The prediction errors that occur are related to AVO attribute anomalies. Second band-pass filtered P-wave impedances, Z_P, and squared S-wave over P-wave velocity ratios, $(V_S/V_P)^2$, are estimated by spectral coherence matching from, respectively, a migrated near-offset sub-stack and the prediction error section. Objective low-frequency contents for both parameters are imposed from well log information and a priori knowledge about the media geometry. One synthetic example and one real North Sea inline illustrate the application of the methods.

PARTIAL COHERENCE ANALYSIS FOR AVO ANOMALY MAPPING

Partial coherence analysis

Our partial coherence technique is an extension of the correlation technique of Thomas et al. (1998). Their technique yielded an optimum scaling factor, the time and phase shifts between two sub-stacks. Our partial coherence technique aims at estimating the optimal filters to predict one offset sub-stack from several other offset sub-stacks in order to have an AVO-orientated approach. The filter designed for one sub-stack takes into account the information brought by the other sub-stacks.

First, when the impedance contrast is not too strong at an interface, the two-term linearized Zoeppritz equation is a good approximation for the P-wave reflection coefficient:

$$R_{P,t}(\theta_t) = R_{P,t}(0) + G_t \sin^2 \theta_t \ , \tag{1}$$

where

$$R_{P,t}(0) = \frac{1}{2}\frac{\partial_t Z_P}{Z_P}, \quad G_t = \frac{1}{2}\frac{\partial_t V_P}{V_P} - 2\gamma^2 \frac{\partial_t \mu}{\mu}. \quad \text{(Wang 1999)} \tag{2}$$

At the interface at two-way traveltime t, $\partial_t V_P/V_P$, $\partial_t Z_P/Z_P$ and $\partial_t \mu/\mu$ are the relative contrasts in P-wave velocity, P-wave impedance, and shear modulus, while γ is the average V_S/V_P ratio; θ_t is the P-wave incidence angle above the interface. With this 2-term approximation only two migrated offset sub-stacks are necessary to predict a third one by means of partial coherence. Let $y_{j,t}$ be the j^{th} offset, effective incidence angle θ_j, sub-stack at two-way traveltime t:

$$y_{j,t} = w_{j,t} * r_t\left(1 + \alpha \sin^2 \theta_j\right) + n_{j,t} \ . \tag{3}$$

The sequence of zero-offset reflection coefficients is r_t and the noise content $n_{j,t}$. The normal moveout stretch is taken into account by considering distinct wavelets $w_{j,t}$ for each angle stack. The constant α is the AVO gradient/intercept ratio (White et al. 1999). From now on, the seismic AVO response of an event shall be called normal whenever

its gradient/intercept ratio remains equal to the background ratio α; any event whose AVO gradient/intercept ratio differs from α shall be called AVO anomalous (Castagna, 1993). Let consider three offset sub-stacks: a near, a mid and a far offset sub-stacks. Partial coherence analysis carried out in a normal AVO zone yields the two filters to be applied to the near and mid offset traces to predict optimally the far traces where AVO is normal. From Bendat and Piersol (1966) and Jenkins and Watt (1968) theory for partial coherence analysis, we established the two filters to be applied to the near and mid traces to minimize the square prediction errors in the far traces (see details in Appendix). The frequency responses of these two filters are:

$$H_1(f) = \frac{\xi_2}{D}\frac{\beta_3(f)}{\beta_1(f)}, \quad H_2(f) = \frac{\xi_1}{D}\frac{\beta_3(f)}{\beta_2(f)}, \tag{4}$$

where

$$D = \xi_1 + \xi_2 + \xi_1\xi_2 \ , \quad \beta_j(f) = \left(1 + \alpha \sin^2 \theta_j\right) W_j(f) \ , \quad j \in \{1, 2, 3\}.$$

The N/S ratio of the j^{th} offset sub-stack is ξ_j; $W_j(f)$ is the Fourier transform of wavelet $w_{j,t}$. The N/S ratio can be measured via multiple coherence analysis. The first fraction, $\xi_j(f)/D$, in equation (4) weights each stack inversely as the S/N ratio. The second factor, $\beta_3(f)/\beta_j(f)$, corrects for any scaling, time and phase shifts relative to the far-offset sub-stack. The predicted far signal is then the reflection signal on far offset sub-stack $\beta_3(f)R(f)$ filtered by a Wiener filter $[\xi_1(f) + \xi_2(f)]/D$ that minimises the mean square prediction error. The slight bias introduced by the filter can be removed by some increase in the noise-induced prediction errors, by measuring the N/S spectra.

As mentioned above, if the coherence analysis is carried out in a zone free of AVO anomalies, the predicted gradient/intercept ratio values are equal to the background ratio value. When the same prediction filters are applied to a zone where AVO anomalies occur, prediction errors highlight deviations of reflection parameters from this background ratio value. In addition to AVO anomalies, the variation in the S/N ratio, the seismic wavelet or the amplitude-offset scaling may cause prediction errors. But unlike AVO anomalies, they produce non-localized and/or uncorrelated with the structure spatial increases in the prediction error power (Thomas 1999). Significant variation in the prediction filters and their frequency contents when the analysis window varies spatially may highlight such effects. As a consequence to predict the normal AVO trend, a coherence analysis needs to be carried out in a window where both angle of incidence and V_S/V_P ratio do not vary much and where the S/N ratio is reasonable.

Accuracy and goodness-of-fit are both relevant to assess of the reliability of a matching process. The "predictability" or proportion of trace energy predicted (*PEP)* defines the goodness-of-fit:

$$PEP = 1 - \frac{\sum_t \left(y_t - \hat{y}_t\right)^2}{\sum_t y_t^2} \ . \tag{5}$$

The energy is measured by sum of squares, y_t is the seismic trace and $\hat{y}_t$ is the estimated filtered sequence. The filter accuracy is measured by the normalised mean square error (*NMSE):*

$$NMSE = \frac{\sum_t \left(\hat{s}_t - s_t\right)^2}{\sum_t s_t^2}. \tag{6}$$

s_t is the actual (modelled) reflection signal, i.e. the signal y_t less the noise n_t, $\hat{s}_t$ is the predicted reflected signal. A filter, which has the minimum *NMSE* with respect to variations in the design parameters will be referred as an optimal filter. It depends strongly on the reliability of the portion of sub-stack used to generate the events (White 1992). The lag window (a symmetric taper equal to 1 at its centre and tapering to 0 at its edges) is used to ensure the existence of the inverse of the auto-correlation matrix. Its length is a determining parameter as it has a direct influence on the result accuracy (Bunch and White 1985). When the lag window length increases, the predictability keeps increasing since the least-square method tends to fit both signal and noise. However the accuracy reaches first a maximum (reducing the windowing bias effect: Bunch and White 1985); it is then degraded progressively (increasing the noise propagation in the filter). We chose the lag window length leading to the best trade-off between *PEP*, *NMSE* as well as filter smoothness.

Prediction errors and AVO anomalies

An AVO anomaly whose gradient is (G_n+ΔG), where G_n is the gradient in an anomaly-free area, introduces an additional signal. We developed the analytic expression of the prediction error, difference between the actual ($y_{3,t}$) and predicted ($\hat{y}_{3,t}$) far-offset sub-stacks (see Appendix):

$$y_{3,t} - \hat{y}_{3,t} = \Delta G_t * \left[\sin^2\theta_3 w_{3,t} - \sin^2\theta_1 h_{1,t} * w_{1,t} - \sin^2\theta_2 h_{2,t} * w_{2,t}\right]. \qquad (7)$$

h_1 and h_2 are the prediction filters, expressed in the frequency domain (H_1 and H_2) by equation (4). ΔG_t is the gradient anomaly sequence located at normal incidence traveltime t.

This partial coherence method presents advantages over other AVO anomaly mapping methods such as the Karhunen-Loéve transform-based methods, e.g. the Nsoga Mahob and Castagna (2002) technique. For instance, as seen later on, our method highlights quantitatively AVO anomalies whether or not they are related to hydrocarbon. It does not assume uncorrelated trace components (White 1980). It compensates for relative differences between the sub-stacks in amplitude scaling, timing and phase. It has also the advantage to have its own QC (White and Barnola 2002). Indeed, as mentioned previously, actual AVO anomalies are normally localised and show some conformity with the structure and lithology interpretation unlike variation in amplitude scaling, S/N ratio, seismic wavelet or residual moveout. Finally the predicted error map, or residual far-offset section, highlights AVO gradient anomalies quantitatively and optimally relative to the background residual far-offset section values. A threshold can be set to distinguish the expected background level from a more significant AVO anomaly by running an F-test for instance on the prediction error section. At this stage a "mask" section can be built to be used later in the inversion process. It has the same number of traces and time-samples as the sub-stacks. Any sample is set to zero. Where the error amplitude power exceeds the fixed threshold, the sample is set to one. One-zone edges are smoothed; existing "outliers" are eliminated.

Two data examples are now considered. The first one is a 51-trace synthetic Class III sand wedge with a gas-leg over a brine-leg, embedded in shale. Its S/N ratio, ratio of the peak amplitude to the rms noise, is 4. The second example is a North Sea 31-trace migrated inline exhibiting a Class IV gas-filled sand reservoir at 900 ms. The partial coherence analysis parameters and results are gathered in Table 1. The left column of Figures 1 and 2 show the residual far-offset section (above) and the mask section (below) in the synthetic and real examples respectively. The interface between

the shale and the gas-filled sand appears as a strong negative (dark blue) anomaly at the top of the wedge in Figure 1 and at 900 ms in Figure 2. The gas-brine contact is visible as a strong positive (red) anomaly at the base of the wedge in Figure 1 and at 910 ms in Figure 2. In the North Sea case two more reflectors exhibit relatively high positive anomalies. First the reflector at 780 ms coincides with an unconformity due to claystone overlying sandstone according to the well log information (solid line in Figure 3, two right plots). Although no gas-fill is expected, the residual far offset section highlights that the interface and the predicted background AVO responses differ. Therefore partial coherence does also highlight AVO anomalies not related to hydrocarbons. The second high-anomaly reflector is above the shale-gas-fill contact around 890 ms. A cause could be the broad decrease in the V_S/V_P ratio log (solid line in Figure 3, right plot), which may indicate a change in lithology compared with the underlying shale.

P-WAVE AND S-WAVE PARAMETER ESTIMATION

To estimate P-wave and S-wave parameters more reliably and speedily than via AVO inversion, a spectral matching technique devised by Walden and White (1998) is considered. It allows noise in the data and errors in the synthetic seismogram to be taken into account when making a well tie. First the data are rescaled in amplitude, time and phase shift. Then noise transmission into the prediction is attenuated with a Wiener filter. We applied this technique to extract Z_P and squared V_S/V_P ratio sections from, respectively, a migrated near-offset sub-stack and a residual far-offset section obtained by partial coherence. The matching equations in the frequency domain are derived from the principle of the least squares assuming that errors in the synthetic and the noise in the data are uncorrelated with each other and with the seismic reflection signal. To steer the match away from optimum prediction towards unbiased prediction, both input and output are considered noisy: the filters between input and output are estimated whereas standard least squares optimise the prediction of output from input. The technique has three main requirements. First, attention must be paid to obtain reliable well logs and to tie the well accurately. A 2-term linearized Zoeppritz equation is still assumed accurate for modelling AVO responses. Second, the inversion to V_S/V_P ratio assumes that Gassmann's fluid-substitution theory (1951) is satisfied within the reservoir area. The datasets and logs of our two examples have been checked for consistency with this fluid-substitution theory within the reservoir area.

P-wave impedance estimation

From equation (1), the closer θ_t to normal incidence, the higher the proportion of P-wave information contained in $R_{P,t}(\theta_t)$. Therefore in the process explained below, an extrapolated normal incidence section, if available, is preferable to the migrated near-offset sub-stack.

Let $x_{1,t}^*$ be the migrated near-offset sub-stack trace that best samples the zone around the well bore. The available well log data, e.g. P-wave velocity and density logs, yield the P-wave impedance $Z_{P,t}$, and reflectivity r_t series at the well location. The first step consists in band-pass filtering r_t to get a frequency-content similar to that of the near-offset trace close to the well location. This is to avoid the amplification of high-frequency noise in the next inversion step. Let b_t be the required band-pass filter. The matching technique is applied to transform the near trace into the b_t-filtered P-wave impedance-log. In a least square sense a filter e_t, which satisfies:

$$x_{1,t}^{*} * e_t \approx Z_{P,t} * b_t \ , \tag{8}$$

is estimated. Then this filter is applied to the whole migrated near-offset sub-stack to yield the corresponding band-pass filtered Z_P section.

To display absolute rather than relative impedance (band-limited impedance contrasts) one needs to add the appropriate low-frequency content to the estimated impedance values. If h_t is the high-cut filter whose high frequency response is identical to that of b_t, the low-frequency content at the well is simply designed by considering the difference between filters h_t and b_t. The absolute P-wave impedance section, $Z_{P,t}^{abs}$, is obtained by adding the band-pass filtered estimate and the low-frequency content extended from the trace at the well to the whole section:

$$Z_{P,t}^{abs} = x_{1,t} * e_t + \left[Z_{P,t} * \left(h_t - b_t \right) \right]_{ext} \ . \tag{9}$$

If there are no major lateral variations in the section, the low-frequency content may be included simply by adding the low-frequency background at the well. However in the case of significant lateral variations, the extension requires building a laterally varying horizon-following low-frequency model. The Z_P log as well as the "normal" Z_P log are extended laterally, following horizons and using any available information concerning the model such as the dip of the layers. The "normal" Z_P log is the Z_P log, where any hydrocarbon has been substituted by brine using the Gassmann fluid substitution theory. Then the "mask-technique" is considered. First, to set Z_P values in AVO-anomalous zones, the mask section is applied to the extended Z_P log section. Second, to set Z_P values in normal-AVO zones, the complementary (1-mask)-section is applied to the extended normal Z_P log section. Both results are added and filtered with the low-pass filter (h_t-b_t). Although objective low-frequency content is obtained with the mask-technique, it is restricted to the information provided by the well(s), i.e. to AVO anomalies crossed by a well. A block diagram in Figure 4 summarizes the process, which is applied to the synthetic model and the North Sea inline. Figures 1 and 2 (above, right) show the predicted sections. Analysis parameters and results are gathered in Table 2. The errors are defined as the ratio of the absolute difference between actual and predicted trace values to the actual trace values. Note that they have been computed in windows larger (516-1108 ms in the real data case) than the analysis windows, i.e. taking into account additional reflectors, because no strong lithology property variation occurs. The maximum errors remain overall less than 9.9 % at the well location (Z_P curves in Figure 3). Therefore reasonable (filtered) Z_P predictions are obtained, even slightly outside the edges of the design window because the lithology properties do not vary much.

V_S/V_P ratio estimation

The prediction error, equation (7), involves the gradient anomaly sequence located at normal incidence traveltime t. We develop the gradient anomaly sequence expression (see the Appendix for details):

$$\Delta G_t = \frac{1}{2} \partial_t \ln\left(\frac{V_P}{V_{P,n}} \right) + 2\left(\gamma_n^2 - \gamma^2 \right) \frac{\partial_t \mu_n}{\mu_n} + 2\gamma^2 \left(\frac{\partial_t \mu_n}{\mu_n} - \frac{\partial_t \mu}{\mu} \right) \ . \tag{10}$$

ln stands for the natural logarithm. The P-wave velocity, the shear modulus and the V_S/V_P ratio values outside the reservoir are denoted by $V_{P,n}$, μ_n and γ_n (n standing for "normal" AVO), while within the reservoir, the values are obtained by adding ΔV_P, $\Delta\mu$, and $\Delta\gamma$ to them to give V_P, μ and γ. In practice ΔG_t at the well location can be estimated

by evaluating the right-side term in brackets in equation (7) using for instance elastic impedances.

Because the well logs are assumed consistent with Gassmann theory in the reservoir area, any change in fluid does not affect the shear modulus value: μ is equal to μ_n and the last term in the above equation is 0.0. As a consequence the residual far-offset section is linearly dependent on the quantity γ^2: the matching technique, applied to the AVO gradient anomaly section enables an estimation of its values. While a band-pass filter (b_t) was designed to get a frequency-content similar for the P-wave reflectivity series to the near-offset sub-stack (Figure 4), b_t is now estimated for a reflectivity series, computed with far elastic impedances rather than acoustic impedances to match the frequency content of the residual far-offset section. The "mask-technique" is applied to normal and non-normal squared velocity-ratio sequences to yield the low-frequency estimate. The square root of the low-frequency content added to the predicted band-pass filtered section provides the corresponding V_S/V_P ratio values. Analysis parameters and results are displayed in Table 2.

The predicted V_S/V_P ratio sections are shown in Figures 1 and 2 (below, right) and predicted values at the well location in Figure 3. As for the predicted Z_P values, the maximal errors in larger windows than the analysis windows remain reasonable at the well location (less than 14 % for the squared velocity ratio). It indicates the reliability of the predicted V_S/V_P ratio, even slightly outside the analysis window. The main reason is again that there is no strong lithology variation within the extended parts of the analysis windows. Note that on the North Sea V_S/V_P section, the event above the gas-fill showing low (blue) velocity-ratio values has already been noticed on the residual far-offset section. A cause can be the broad decrease in the V_S/V_P log just above the gas-fill (Figure 3, right), which may have been worsened by wavelet side-lobe effects.

DISCUSSION

These results are now compared with parameter sections obtained via a hard-constrained AVO inversion followed by a constraint-induced bias-removal step to make the results quantitative (Barnola and White 2001). Figure 5 shows Z_P and V_S/V_P ratio sections obtained via AVO inversion constrained with a Gardner-type relation ($\rho = kV_P^n$, where k and n are two constant parameters) in the North Sea inline case. These sections have not been corrected for the constraint-induced biases. First, from a qualitative point of view, partial coherence predictions (Figure 2, right column) are much less noisy than AVO inversion retrieved parameters, especially V_S/V_P ratios. The P-wave impedance section retrieved by coherence matching is improved compared with inversion results. Indeed it is smoother and more layers are visible, e.g. the high P-wave impedance (red) layers below the gas-fill sand. The tuning effect that initially distorted gas-fill related amplitudes seems attenuated. Second, from a quantitative point of view, results after the AVO inversion are biased by the Gardner-type constraint: they need an extra correction step that Barnola and White (2001) suggested. Figure 6 shows the P-wave impedance and V_S/V_P ratio values at the well location before and after the removal of the Gardner constraint-induced biases in the synthetic and real data examples. Even after correction, errors on the estimated parameters remain non-negligible, especially for S-wave related parameters. Indeed on V_S/V_P ratio the errors exceed 50 % in the synthetic case and 20 % in the North Sea inline case.

CONCLUSIONS

Via partial coherence, we designed multichannel filters to predict a migrated far-offset sub-stack from migrated near- and mid-offset sub-stacks in a zone where AVO was "normal". Localised prediction errors occurred whenever the same filters were applied in zones exhibiting AVO anomalies. Partial coherence provided an AVO anomaly map, which had its own QC. Only consistent - not absolute - amplitude scaling, timing and phase were required. Variation in the S/N ratio, the seismic wavelet or the amplitude-offset scaling might cause prediction errors but they would be non-localised and/or show some incoherence with the lithology and structure interpretation. To map a reservoir area, this partial coherence-based method did not require any preliminary interpretation of seismic sections. Furthermore in one synthetic example and one real North Sea data case the prediction errors allowed anomalies in AVO gradient to be tested and distinguished from the background. The evaluation of the AVO gradient anomaly at the well location can be done using elastic impedances.

Then we applied a spectral coherence technique from Walden and White (1998) to invert a migrated near-offset sub-stack to band-pass filtered P-wave impedances. We used the linear dependence of the AVO gradient anomaly on the squared V_S/V_P ratio to invert the residual far-offset section obtained via partial coherence to band-pass filter squared velocity ratio. A "mask-technique" was designed to get an objective low-frequency content for both estimated parameters from well log information and a priori knowledge on the media geometry. The advantage of our technique is to invert AVO anomalies only. We showed in the North Sea inline example that predicted parameters were dramatically improved, especially S-wave impedances, compared with the ones retrieved by hard-constrained AVO inversion. At the well location the errors for the two estimates were less than 9.9 % for P-wave impedances and less than 14 % for $(V_S/V_P)^2$ ratios. Slightly outside the analysis windows, because there was no strong variation within the lithology properties, the prediction errors remain reasonable as well.

As presented the inversion to V_S/V_P ratio values required that all log values remained Gassmann-consistent within the reservoir. As a consequence the parameter sections did not need any further correction as they did after a hard-constrained inversion. However the estimation of an objective low-frequency content for both P-wave impedances and $(V_S/V_P)^2$ ratios was restricted to lithologies crossed by a well.

Finally a more elaborate method of inversion is needed in the case of very strong impedance contrasts when the 2-term linearized Zoeppritz equation for the P-wave reflection coefficient is no longer correct. An iterative method or a full Zoeppritz inversion could be used instead.

ACKNOWLEDGEMENTS

We thank BP-Amoco and Texaco Britain Limited for their support of this research and Venture Petroleum for permission to show their data.

APPENDIX

Partial coherence theory: prediction of the far-offset traces from the near- and mid-offset traces

Bendat and Piersol (1966) and Jenkins and Watts (1968) gave the basic theory for partial coherence analysis. They introduced the residual conditioned spectral matrix to compute the residual spectra when one tried to predict data from other sets of data. In the case of one dataset to be predicted from two other datasets, its expression is:

$$S_{13/2}(f)=\begin{pmatrix}\Phi_{33/2}(f) & \Phi_{31/2}(f)\\ \Phi_{13/2}(f) & \Phi_{11/2}(f)\end{pmatrix}=A-BD^{-1}C \ . \qquad \text{(A1)}$$

The indexes stand for the migrated near- (1), mid- (2) and far- (3) offset sub-stacks. A, B, C and D are matrices defined by:

$$A=\begin{pmatrix}\Phi_{33} & \Phi_{31}\\ \Phi_{13} & \Phi_{11}\end{pmatrix}, \quad B=\begin{pmatrix}\Phi_{32}\\ \Phi_{12}\end{pmatrix}, \quad C=\begin{pmatrix}\Phi_{23} & \Phi_{21}\end{pmatrix}, \quad \text{and} \quad D=\begin{pmatrix}\Phi_{22}\end{pmatrix}. \qquad \text{(A2)}$$

Φ_{jj} is the auto-spectrum of the angle stack j, Φ_{jk} is the cross-spectrum of angle stacks j and k:

$$\Phi_{jj}(f)=\left|\beta_j(f)\right|^2\Phi_{rr}(f)+\Psi_{jj}(f), \quad \text{and} \quad \Phi_{jk}(f)=\beta_j^*(f)\beta_k(f)\,\Phi_{rr}(f), \qquad \text{(A3)}$$

where: $\beta_j(f)=\left(1+\alpha\sin^2\theta_j\right)W_j(f)$, $(j, k)\,\epsilon\,\{1, 2, 3\}^2$.

The notations are similar to the ones used in equation (3). Φ_{rr} and $\Psi_{jj}(f)$ are the power spectra of the reflectivity series r_t and of the noise $n_{j,t}$ respectively. $W_j(f)$ is the Fourier transform of wavelet $w_{j,t}$.

The frequency response for the first input after conditioning on the second input is (Bendat and Piersol 1966):

$$H_1(f)=\frac{\Phi_{13/2}(f)}{\Phi_{11/2}(f)} \ . \qquad \text{(A4)}$$

With the notations introduced by equation (A3), we computed first $\Phi_{13/2}$ and $\Phi_{11/2}$ expressions with equations (A1) and (A2) and second $H1$ and $H2$ expressions using equation (A4). The filters to predict the migrated far-offset sub-stack from the near- and mid-offset sub-stacks are therefore:

$$H_1(f)=\frac{\xi_2}{D}\frac{\beta_3(f)}{\beta_1(f)}, \quad H_2(f)=\frac{\xi_1}{D}\frac{\beta_3(f)}{\beta_2(f)}, \quad \text{where} \quad D=\xi_1+\xi_2+\xi_1\xi_2 \ . \qquad \text{(A5)}$$

With the N/S ratio: $\xi_j=\dfrac{\Psi_{jj}(f)}{\left|\beta_j(f)\right|^2\Phi_{rr}(f)}$, $j\,\epsilon\,\{1,2\}$. (A6)

Prediction error analytic expression

With the notation introduced in equation (3), the gradient series G_t in a normal AVO zone satisfies: $G_t=\alpha r_t$. (A7)

When AVO anomalies are encountered, the gradient becomes $G_t+\Delta G_t$, where ΔG_t is the AVO gradient anomaly series. Using the equation (3) notations, within a normal AVO zone, the predicted ($\hat{y}_{3,t}$) and actual ($y_{3,t}$) migrated far-offset sub-stacks are very similar:

$$y_{3,t}(G_t)\approx\hat{y}_{3,t}(G_t)=h_{1,t}*y_{1,t}(G_t)+h_{2,t}*y_{2,t}(G_t). \qquad \text{(A8)}$$

$h_{1,t}$ and $h_{2,t}$ are the two filters in the time domain designed by means of partial coherence (equation (4)). In presence of AVO anomalies, both predicted and far-offset sub-stacks differ. The expression for the predicted far-offset sub-stack in that case is:

$$\hat{y}_{3,t}(G_t + \Delta G_t) = h_{1,t} * y_{1,t}(G_t + \Delta G_t) + h_{2,t} * y_{2,t}(G_t + \Delta G_t). \quad \text{(A9)}$$

Equation (A9) is developed:

$$\hat{y}_{3,t}(G_t + \Delta G_t) = \left[h_{1,t} * w_{1,t} + h_{2,t} * w_{2,t}\right] * r_t + \left[w_{1,t} * h_{1,t} \sin^2\theta_1 + w_{2,t} * h_{2,t} \sin^2\theta_2\right] * G_t$$
$$+ \left[w_{1,t} * h_{1,t} \sin^2\theta_1 + w_{2,t} * h_{2,t} \sin^2\theta_2\right] * \Delta G_t + h_{1,t} * n_{1,t} + h_{2,t} * n_{2,t}.$$

Then it is simplified with equation (A8):

$$\hat{y}_{3,t}(G_t + \Delta G_t) = y_{3,t}(G_t) + \Delta G_t * \left[w_{1,t} * h_{1,t} \sin^2\theta_1 + w_{2,t} * h_{2,t} \sin^2\theta_2\right]. \quad \text{(A10)}$$

On the other hand, from equation (3):

$$y_{3,t}(G_t + \Delta G_t) \approx y_{3,t}(G_t) + \Delta G_t * w_{3,t} \sin^2\theta_3. \quad \text{(A11)}$$

The difference between equations (A11) and (A10) yields the prediction error time-sequence expression:

$$y_{3,t} - \hat{y}_{3,t} = \Delta G_t * \left[w_{3,t} \sin^2\theta_3 - w_{1,t} * h_{1,t} \sin^2\theta_1 - w_{2,t} * h_{2,t} \sin^2\theta_2\right]. \quad \text{(A12)}$$

AVO gradient anomaly expression

The P-wave velocity, the shear modulus and the V_S/V_P ratio values outside the reservoir are denoted by $V_{P,n}$, μ_n and γ_n (n standing for "normal" AVO). Within the reservoir, the values are obtained by adding ΔV_P, $\Delta\mu$, and $\Delta\gamma$ to them to give V_P, μ and γ. With the gradient expression given by equation (2) the difference between the gradient and the normal gradient series is computed at traveltime t:

$$\Delta G_t = G_t - G_t^n = \frac{1}{2}\left(\frac{\partial_t V_P}{V_P} - \frac{\partial_t V_{P,n}}{V_{P,n}}\right) + 2\left(\gamma_n^2 \frac{\partial_t \mu_n}{\mu_n} - \gamma^2 \frac{\partial_t \mu}{\mu}\right). \quad \text{(A13)}$$

The right side first term in equation (A13) is developed:

$$\frac{\partial_t V_P}{V_P} - \frac{\partial_t V_{P,n}}{V_{P,n}} = \frac{V_{P,n}\partial_t V_P - V_P \partial_t V_{P,n}}{V_P V_{P,n}} = \partial_t \ln\left(\frac{V_P}{V_{P,n}}\right). \quad \text{(A14)}$$

ln stands for the natural logarithm. The right side second term in equation (A13) is rearranged:

$$\gamma_n^2 \frac{\partial_t \mu_n}{\mu_n} - \gamma^2 \frac{\partial_t \mu}{\mu} = \left(\gamma_n^2 - \gamma^2\right)\frac{\partial_t \mu_n}{\mu_n} + \gamma^2\left(\frac{\partial_t \mu_n}{\mu_n} - \frac{\partial_t \mu}{\mu}\right). \quad \text{(A15)}$$

Back to equation (A13) with the new expressions (A14) and (A15) for the right side:

$$\Delta G_t = \frac{1}{2}\partial_t \ln\left(\frac{V_P}{V_{P,n}}\right) + 2\left(\gamma_n^2 - \gamma^2\right)\frac{\partial_t \mu_n}{\mu_n} + 2\gamma^2\left(\frac{\partial_t \mu_n}{\mu_n} - \frac{\partial_t \mu}{\mu}\right). \quad \text{(A16)}$$

REFERENCES

Barnola A-S. and White R.E. 2001. Gardner's relations and AVO inversion. *First Break* **19**, 607-611.

Bendat J.S. and Piersol A.G. 1966. *Random Data, Analysis and Measurement Procedures*. 2nd ed., New York: John Wiley and Sons.

Bunch A.W.H. and White R.E. 1985. Least-squares filters without transient errors - An examination of the errors in least-squares filter design. *Geophysical Prospecting* **33**, 657-673.

Castagna J.P. 1993. Petrophysical imaging using AVO. *The Leading Edge* **12**, 172-178.

Gassmann F. 1951. Über die Elastizität poröser Medien. *Vierteljahrsschrift der Naturforschenden. Gesellschaft in Zürich* **96,** 1-23.

Jenkins G.M. and Watts D.G. 1968. *Spectral Analysis and its applications*. Holden-Day, San Francisco.

Nsoga Mahob P. and Castagna J.P. 2002. AVO hodograms and polarization attributes. *The Leading Edge* **21**, 18-27.

Thomas R.D. 1999. *Quantitative controls on the quality of pre-stack seismic data for attribute analysis*. Ph.D. Thesis, Birkbeck College, University of London.

Thomas R.D., Castoro A. and White R.E. 1998. QC of prestack seismic processing and attribute extraction. 60th EAGE meeting, Leipzig, Germany, Expanded Abstracts, **2-54**.

Walden A.T. and White R.E. 1998. Seismic wavelet estimation: A frequency domain solution to a geophysical noisy-input-output problem. *IEEE Transaction on Geoscience and remote sensing* **36**, 287-297.

Wang Y. 1999. Approximations to the Zoeppritz equations and their use in AVO analysis. *Geophysics* **64**, 1920-1927.

White R.E. and Barnola A-S. 2002. Coherence methods in AVO detection and quality control. 64th EAGE meeting, Florence, Italy, Expanded Abstracts, **G-13**.

White R.E., Simm R. and Castoro A. 1999. A systematic approach to AVO analysis. 61st EAGE meeting, Helsinki, Finland, Expanded Abstracts, **6-53**.

White R.E. 1992. *Matching noisy synthetic seismograms and seismic data*. Birkbeck College Exploration Seismology Research Group, Internal Report.

White R.E. 1980. Partial coherence matching of synthetic seismograms with seismic traces. *Geophysical Prospecting* **28**, 333-358.

LIST OF FIGURES

Figure 1. Synthetic model: Residual far-offset section (above, left), mask section (below, left), predicted filtered P-wave impedances (above, right) and V_S/V_P ratios (below, right). Impedances are in (km/s)*(g/cm^3).

Figure 2. North Sea inline: Residual far-offset section (above, left), mask section (below, left), predicted filtered P-wave impedances (above, right) and V_S/V_P ratios (below, right). Impedances are in (km/s)*(g/cm^3).

Figure 3. P-wave impedance and V_S/V_P ratio values at the well location for the synthetic model (two first panels) and the North Sea inline (two last panels). The solid lines are the actual parameter filtered values. The dotted lines are the predicted filtered values. Impedances are in (km/s)*(g/cm^3).

Figure 4. Block diagram of the strategy to quantitatively estimate P-wave impedances.

Figure 5. North Sea inline: P-wave impedance (above) and V_S/V_P ratio (below) sections retrieved via Gardner-constrained AVO inversion. Impedances are in (km/s)*(g/cm^3).

Figure 6. P-wave impedance and V_S/V_P ratio values at the well location from the inversion with a Gardner-type relation as a hard constraint. The synthetic model (two first panels) and the North Sea inline (two last panels) cases are shown. The solid lines are the actual parameter values. The dotted lines are the predicted values after removal of the Gardner relation-induced biases. Impedances are in (km/s)*(g/cm^3). Note that these logs have not been filtered and that the well log values are displayed versus traveltime in the synthetic case and versus depth in the North Sea case.

LIST OF TABLES

Table 1. Analysis window and best-fit information for the partial coherence analyses of the synthetic model and the North Sea inline.

Table 2. Analysis window, frequency content, PEP and average error at the well location for the predicted P-wave impedances and squared V_S/V_P ratios.

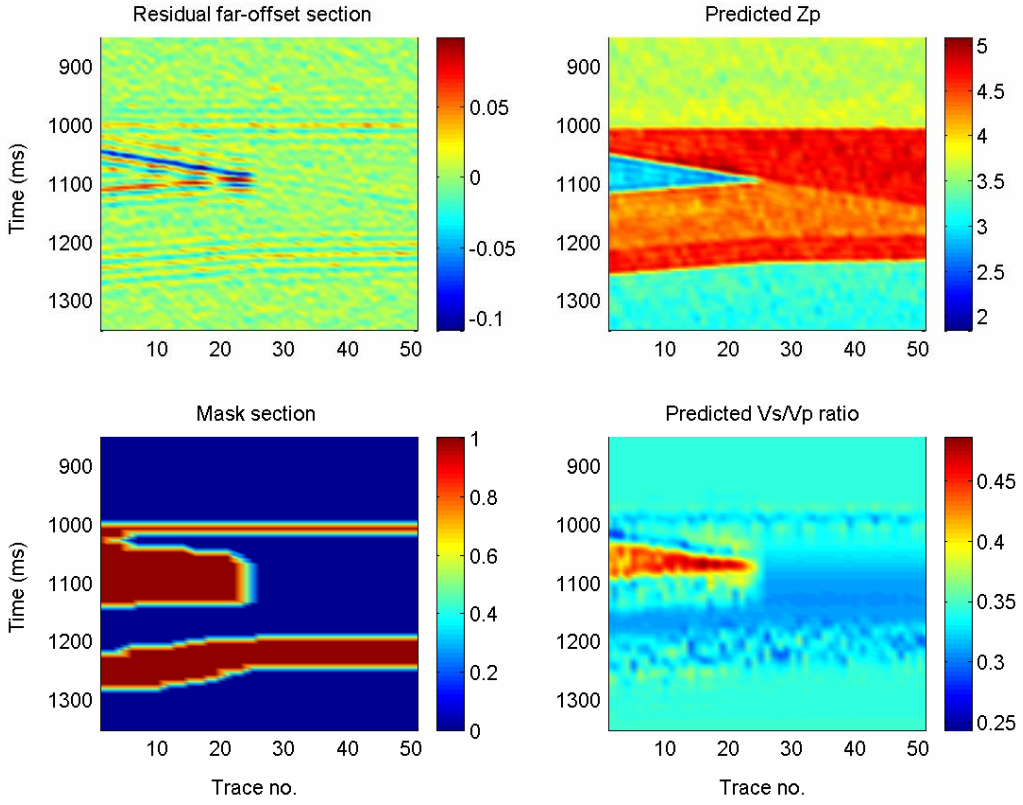

Figure 1. Synthetic model: Residual far-offset section (above, left), mask section (below, left), predicted filtered P-wave impedances (above, right) and V_S/V_P ratios (below, right). Impedances are in (km/s)*(g/cm^3).

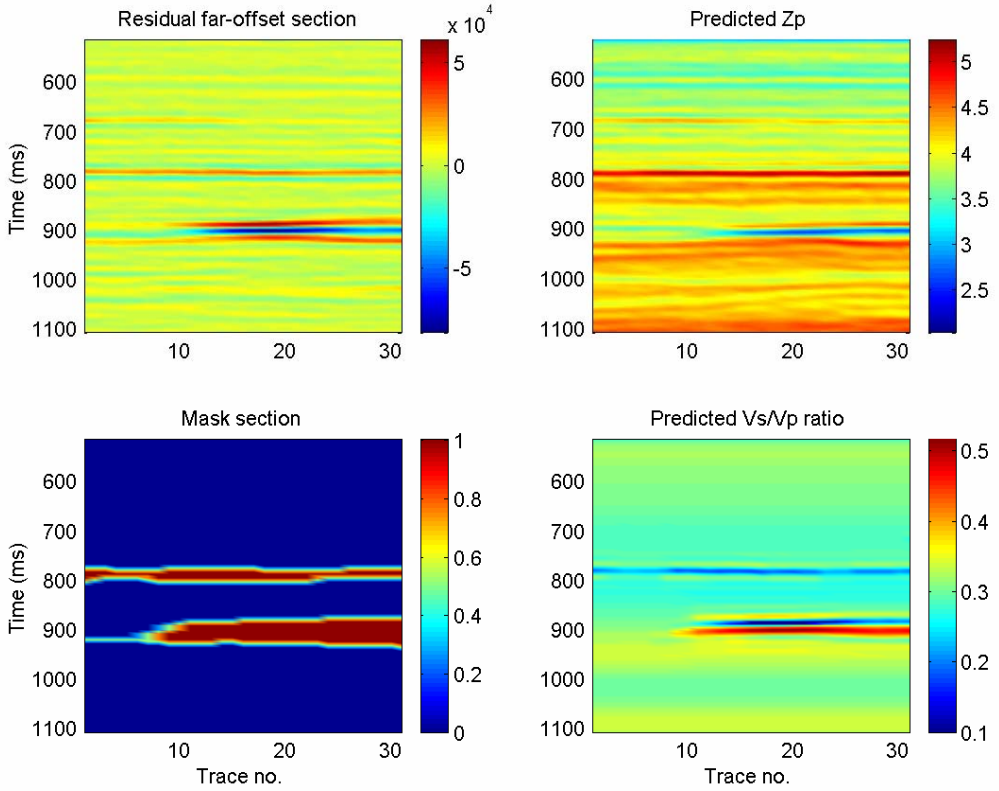

Figure 2. North Sea inline: Residual far-offset section (above, left), mask section (below, left), predicted filtered P-wave impedances (above, right) and V_S/V_P ratios (below, right). Impedances are in (km/s)*(g/cm^3).

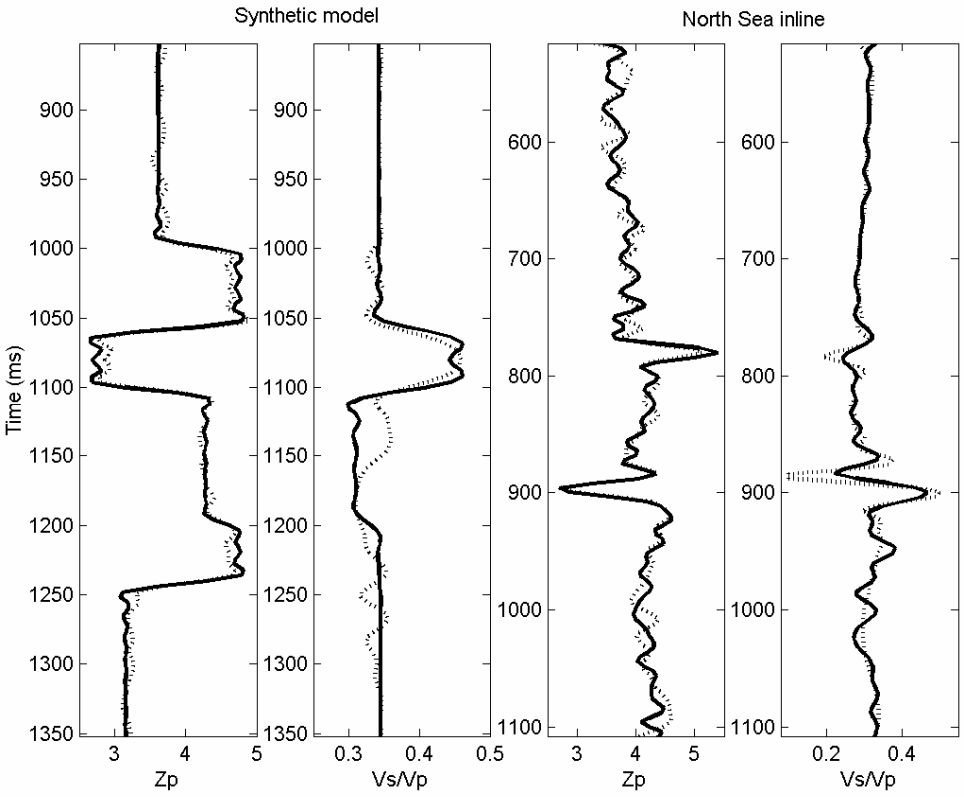

Figure 3. P-wave impedance and V_S/V_P ratio values at the well location for the synthetic model (two first panels) and the North Sea inline (two last panels). The solid lines are the actual parameter filtered values. The dotted lines are the predicted filtered values. Impedances are in (km/s)*(g/cm^3).

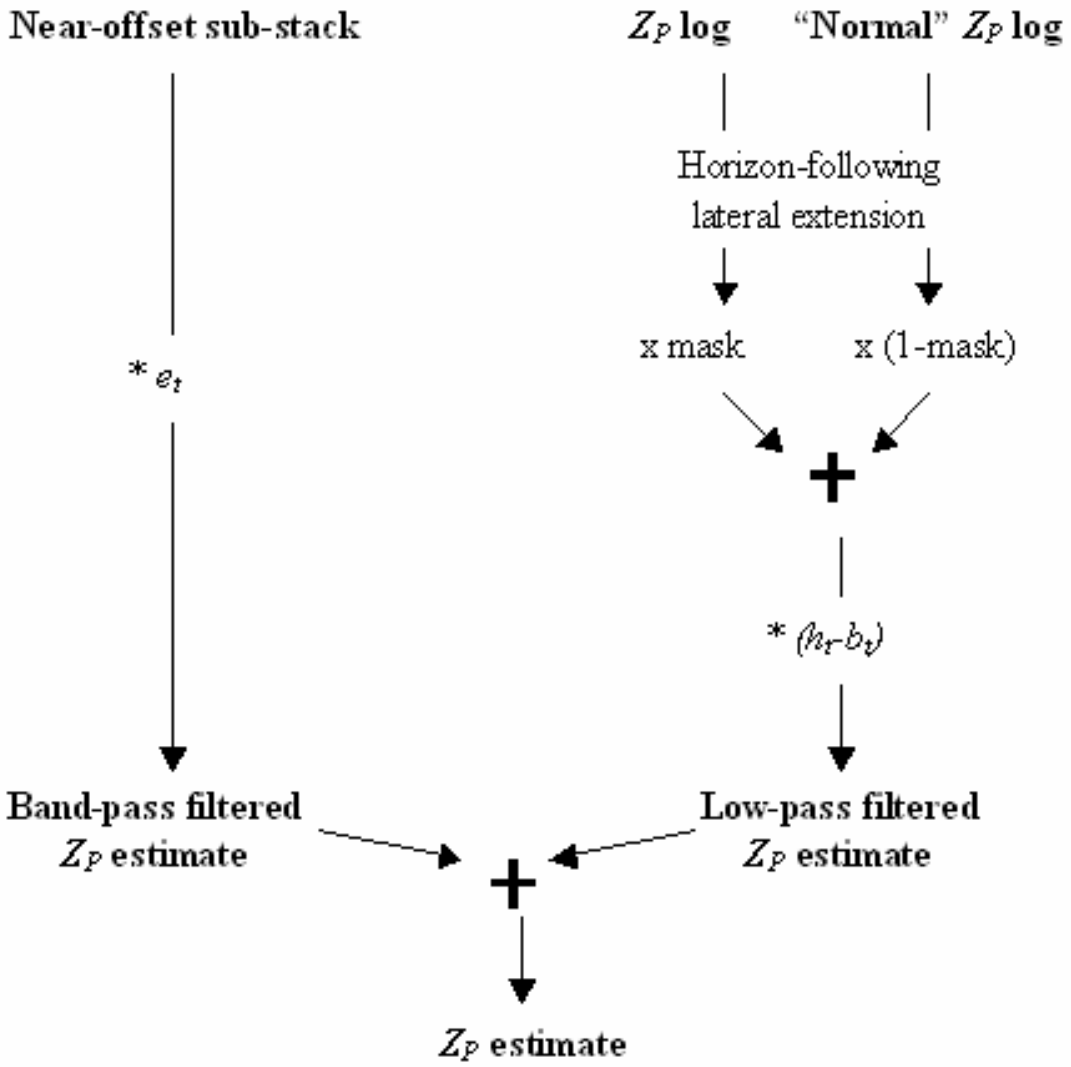

Figure 4. Block diagram of the strategy to quantitatively estimate P-wave impedances.

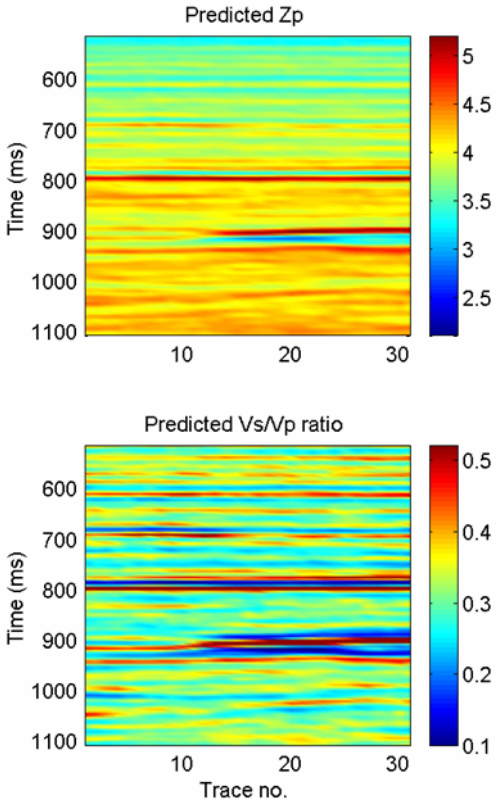

Figure 5. North Sea inline: P-wave impedance (above) and V_S/V_P ratio (below) sections retrieved via Gardner-constrained AVO inversion. Impedances are in (km/s)*(g/cm^3).

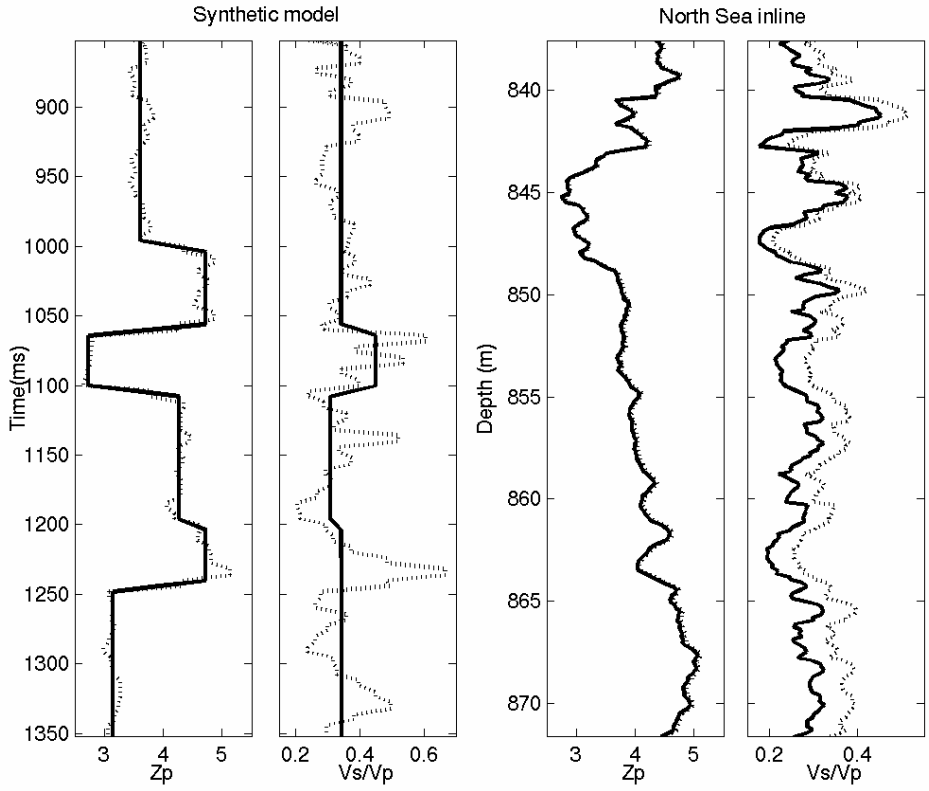

Figure 6. P-wave impedance and V_S/V_P ratio values at the well location from the inversion with a Gardner-type relation as a hard constraint. The synthetic model (two first panels) and the North Sea inline (two last panels) cases are shown. The solid lines are the actual parameter values. The dotted lines are the predicted values after removal of the Gardner relation-induced biases. Impedances are in (km/s)*(g/cm^3). Note that these logs have not been filtered and that the well log values are displayed versus traveltime in the synthetic case and versus depth in the North Sea case.

	Analysis window		*PEP* (trace)
	Time	Traces	
Synthetic model	990-1230 ms	28-50	88.3 % (48)
North Sea inline	608-848 ms	10-25	88.2 % (17)

Table 1. Analysis window and best-fit information for the partial coherence analyses of the synthetic model and the North Sea inline.

	Analysis window		Predicted parameter	Frequency content	*PEP* (trace)	Average error
	Time (ms)	Traces				
Synthetic model	990-1230	7-13	Z_P	0-64 Hz	70.0 % (9)	2.0 %
			$(V_S/V_P)^2$	0-45 Hz	79.0 % (9)	3.1 %
North Sea inline	700-940	1-31	Z_P	0-56 Hz	79.8 % (17)	2.9 %
			$(V_S/V_P)^2$	0-41 Hz	86.7 % (25)	3.4 %

Table 2. Analysis window, frequency content, PEP and average error at the well location for the predicted P-wave impedances and squared V_S/V_P ratios.